Carbon 170 (2020) 589–599

Contents lists available at ScienceDirect

Carbon

journal homepage: www.elsevier.com/locate/carbon

Research Article

Anisotropic spall behavior of CNT/2024Al composites under plate impact

J.C. Cheng [a, 1], H.W. Chai [b, 1], G.L. Fan [c], Z.Q. Li [c], H.L. Xie [d], Z.Q. Tan [c, *], B.X. Bie [a, **], J.Y. Huang [b], S.N. Luo [a]

[a] School of Materials Science and Engineering, Southwest Jiaotong University, Chengdu, Sichuan, 610031, PR China
[b] The Peac Institute of Multiscale Sciences, Chengdu, Sichuan, 610031, PR China
[c] State Key Laboratory of Metal Matrix Composites, School of Materials Science and Engineering, Shanghai Jiao Tong University, Shanghai, 200240, PR China
[d] Shanghai Institute of Applied Physics, Chinese Academy of Science, Shanghai, 201204, PR China

ARTICLE INFO

Article history:
Received 16 May 2020
Received in revised form
27 July 2020
Accepted 3 August 2020

Keywords:
CNT/2024Al composite
Hugoniot elastic limit
Spall strength
Computed tomography

ABSTRACT

Plate impact experiments are conducted on the carbon nanotube (CNT) reinforced 2024Al composite fabricated by flake powder metallurgy and hot extrusion, to investigate the effects of microstructural anisotropy on its dynamic deformation and damage, as well as the role of CNTs. Three loading directions are explored with the loading axis being parallel to the extrusion, transverse or normal direction. Free-surface velocity histories are measured to evaluate the mechanical properties and damage processes, including the Hugoniot elastic limit (HEL; ~0.8 GPa) and dynamic spall strengths (1.4 – 1.9 GPa). Postmortem samples are characterized with synchrotron X-ray computed tomography and scanning electron microscopy. The microstructural anisotropy of the composite (in terms of the orientation of lamellar microstructures) has a negligible effect on HEL but induces an anisotropy in spall strengths; spall strength is the highest for loading along the extrusion direction, the long axis of the lamellar microstructures. CNTs appear to increase the spall strengths of the 2024Al matrix, in contrast to other reinforcing fibers/particles. The crack propagation direction and damage features can be correlated with collinear propagation of microcracks following the lamellar microstructures.

© 2020 Elsevier Ltd. All rights reserved.

1. Introduction

Carbon nanotubes (CNTs) with large aspect ratios have emerged as an ideal reinforcement for composites due to their superior mechanical, thermal and electrical properties, and light weight [1–6]. Integration of CNTs with light metals, such as aluminum and its alloys, may produce strong but light composites for aeronautics and aerospace applications [7,8], where strength increase and weight reduction are the first priority. The impact response [9] of CNT-reinforced aluminum matrix composites (AMCs) is highly relevant to such applications where impact events or accidents (e.g., bird strike and space debris) are inevitable [10,11]. A thorough understanding of impact deformation and damage is helpful for a better, safer usage of CNT-reinforced AMCs, and materials/structural design.

Extensive studies have been devoted to CNT-reinforced AMCs in the past decades, including fabrication [12,13], and mechanical properties and strengthening mechanisms under quasi-static loading [14,15]. CNT-reinforced AMCs generally exhibits higher strength than its aluminum matrix under quasi-static loading conditions [16,17]. In particular, both strength and ductility can be increased for CNT-reinforced AMCs synthesized by flake powder metallurgy, upon the balance among CNT dispersion, structural integrity and interfacial bonding [18–21]. However, impact response of CNT-reinforced AMCs is underexplored, especially under plate impact loading. The local strain rate in bird strike and space-debris impact ranges from 10^4 to 10^8 s^{-1} [22,23], beyond the reach of conventional dynamic loading apparatus like drop weight and split Hopkinson bars [24,25]. It is highly desirable to explore the response of CNT-reinforced AMCs under plate impact, including new data on deformation and damage, and underlying mechanisms.

A key figure of merit for evaluating composites against plate impact loading is dynamic spall strength [26], the fracture stress

* Corresponding author.
** Corresponding author.
E-mail addresses: tanzhanqiu@sjtu.edu.cn (Z.Q. Tan), bxbie@swjtu.edu.cn (B.X. Bie).
[1] These authors contribute equally to this work.

https://doi.org/10.1016/j.carbon.2020.08.007
0008-6223/© 2020 Elsevier Ltd. All rights reserved.

under high strain rate tension induced by opposing rarefaction waves. However, the spall behavior of CNT-reinforced AMCs under plate impact loading has not been reported yet. A considerable number of studies have addressed spallation of AMCs with particle or non-carbon fiber reinforcements [27–31]. For example, the Al_2O_3-particle or fiber reinforced AMCs were found to exhibit lower spall strengths than their metal matrix, for such reasons as the weak particle-matrix interface in Al_2O_3-particle reinforced 6061Al-T6 [28], interparticle porosity in Al_2O_3-nanoparticle (10 wt%) reinforced 1013Al [31], and lack of ideal parallel fiber construction in Al_2O_3-fiber (50 vol%) reinforced 6061Al-T4 [29]. Concerning the deformation/failure mechanisms, previous studies were mainly based on two-dimensional surface measurements, while three-dimensional internal characterizations of damage under impact loading was rarely reported, inhibiting a comprehensive understanding of anisotropy and heterogeneity in deformation and damage. With the fast development of synchrotron sources, micro X-ray computed tomography (XCT) can provide high resolution (~1 μm) measurements of internal damage [32–36], but has not been applied to CNT-reinforced AMCs.

In this work, high strain-rate deformation and spall damage of CNT-reinforced 2024Al (CNT/2024Al) composite is investigated under plate impact loading along three different directions (ED: extrusion direction; TD: transverse direction; ND: normal direction). Two different impact velocities (~240 m s^{-1} and ~330 m s^{-1}) are explored to achieve different deformation and damage degrees in composite samples. Free-surface velocity histories are measured to derive the Hugoniot elastic limit (HEL) and spall strength. Shock-recovered samples are characterized with synchrotron XCT and scanning electron microscopy (SEM) to obtain spatial distributions and morphologies of cracks. The microstructure–property relationships and underlying mechanisms are discussed.

2. Materials and experiments

2.1. Materials

The CNT/2024Al composite is fabricated with a flake powder metallurgy route. Multi-walled CNTs are 15–40 nm in diameter and 1–5 μm in length. The average diameter of the Al powders is ~18 μm. Cu and Mg flake powders are approximately 4 μm and 14 μm in diameter, and 0.16 μm and 1.2 μm in thickness, respectively. These raw materials are 99.9 wt% purity.

Powder processing is based on the shift-speed ball milling (SSBM), including low-speed ball milling (LSBM) and high-speed ball milling (HSBM) (Fig. 1a). The SSBM is conducted in a planetary ball mill in a stainless-steel jar filled with Ar atmosphere (1 atm). The revolution radius and rotation radius are 300 mm and 90 mm, respectively. The diameter of balls is around 8 mm. The powder mass is 500 g, with a ball-to-powder mass ratio of about 20:1. During the LSBM process, 1.5 wt% CNTs and 93.5 wt% pure Al powders are mixed with 0.5 wt% stearic acid (analytical reagent), milled at a constant speed of 135 rpm for 8 h to disperse CNTs effectively. At the HSBM stage, 4.0 wt% Cu and 1.0 wt% Mg flake powders are added to the milling jar and milled at a constant speed of 270 rpm for 1 h to obtain cold welded particles. The morphology of the CNT/Al flake powders after LSBM and the CNT/Al–Cu–Mg particles after HSBM are presented in Fig. 1c and d, respectively. Fig. 1e indicates that CNTs (marked by arrows) are uniformly dispersed on the surfaces of the CNT/Al–Cu–Mg particles. After ball milling, the mixed particles are cold pressed into cylinders (inner diameter 120 mm) at 500 MPa, and then hot extruded into 60 mm × 18 mm plates (Fig. 1b) after being sintered in vacuum at 570°C for 4 h. The composite plates are supposed to exhibit lamellar microstructures after hot extrusion, as illustrated in Fig. 1b. These plates are further processed via solution treatment at 530°C for 3 h with an electric resistance furnace, and then quenched rapidly in ice water. Artificial aging treatment is performed on the plates at 130°C for 24 h in an electric resistance furnace with an air atmosphere.

The CNT/2024Al composite has a bulk density $\rho_0 = 2.81 \pm 0.01$ g cm^{-3} as measured with the Archimedean method. The sound velocities of the material are obtained by ultrasonic measurements [37]. Each measurement is repeated three times to calculate its averages and standard deviations. The longitudinal sound velocities are 6669±4, 6640±8 and 6620±3 m s^{-1}, while the transverse sound velocities are 3348±7, 3327±9 and 3342±6 m s^{-1}, along the ED, TD

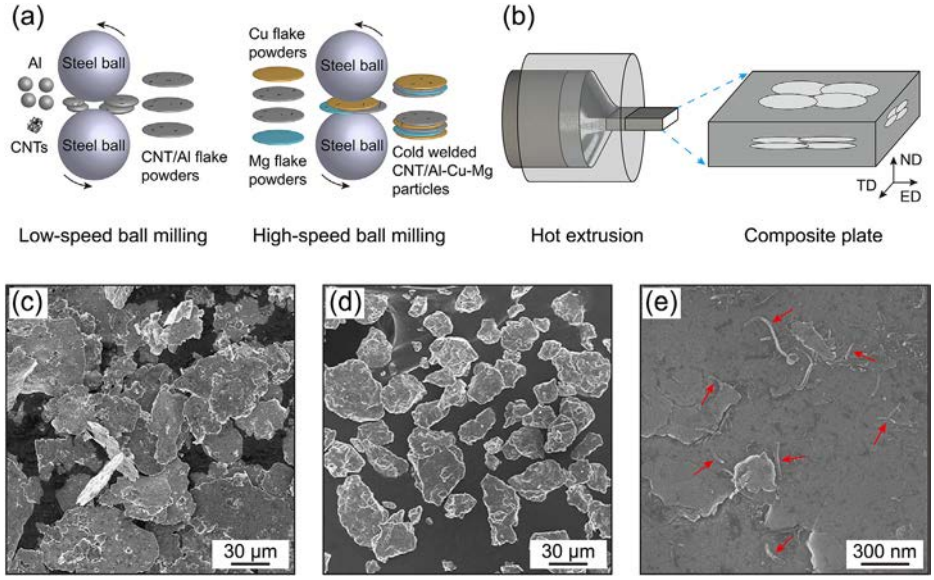

Fig. 1. (a) Illustration of the shift-speed ball milling (SSBM) processing of CNT/Al powders and CNT/Al–Cu–Mg particles. (b) Hot extrusion process and a schematic diagram of the resultant CNT/2024Al composite plate. The ellipses in the composite plate depict the anisotropic morphology of the CNT/Al–Cu–Mg particles observed in three directions. (c) Micrograph of the CNT/Al flake powders after low-speed ball milling (LSBM). (d) Micrograph of the CNT/Al–Cu–Mg particles after high-speed ball milling (HSBM). (e) Dispersion of CNTs (marked by arrows) on the surface of the CNT/Al–Cu–Mg particles. ED: extrusion direction; TD: transverse direction; ND: normal direction. (A colour version of this figure can be viewed online.)

and ND, respectively. The bulk sound velocity (C_B) and Poisson's ratio (ν) calculated from the average values of C_L (6643±22 m s^{-1}) and C_T (3339±11 m s^{-1}) are C_B = 5410±36 m s^{-1} and ν = 0.331±0.003, respectively.

2.2. Microstructural characterizations

The CNT/2024Al composite samples cut from the bulk plate after artificial aging (i.e. as-received) are used for initial microstructural characterizations. X-ray diffraction (XRD) is performed with a Panalytical X-ray diffractometer, and the equipment parameters can be found in Ref. [38]. The available scattering angle (2θ) ranges from 10° to 90°. Raman spectroscopy is used to identify CNTs in the as-received CNT/2024Al composite, with a 532 nm diode-pumped solid-state laser in the spectral range from 400 cm^{-1} to 1800 cm^{-1}. For energy dispersive spectroscopy (EDS) and electron backscattered diffraction (EBSD), the samples are mechanically ground and polished with 1 μm and 0.3 μm Al_2O_3 particles (for EDS), and then electropolishing is conducted in a solution of 10 vol% perchloric acid and 90 vol% ethanol at 25 V and −25°C using a Cu rod and the sample as electrodes (for EBSD). EDS and EBSD characterizations are performed with an FEI Quanta 250 SEM with Oxford EDS and EBSD detectors. The working voltage is 30 kV, while the working distance is 15 mm. An additional 70° tilt is applied for EBSD. Microstructures of Al, CNTs and Al_4C_3 are characterized by high-resolution transmission electron microscopy (HR-TEM) at 200 kV. TEM samples are prepared by mechanical polishing to thickness ~40 μm, and then punched into discs with a 3-mm diameter; final twin-jet electropolishing is carried out by Struers TenuPol-5.

The XRD pattern of the as-received CNT/2024Al composite shows strong Al but weak Al_2Cu and Al_4C_3 diffraction peaks (Fig. 2a); the presence of Al_4C_3 peaks suggests the reaction of CNTs and Al, consistent with previous observations [14,16]. The absence of carbon and Al_2CuMg diffraction peaks may be attributed to their low contents [16,39,40]. The Raman spectrum in Fig. 2b also indicates the formation of Al_4C_3 in CNT/2024Al, with characteristic peaks at 492 cm^{-1} and 863 cm^{-1} [41]. Meanwhile, the Raman peaks of CNTs are also observed at 1332 cm^{-1} (D-band) and 1604 cm^{-1} (G-band) [42].

A backscattered electron image and corresponding EDS mappings of Al, Cu and Mg elements of the as-received CNT/2024Al are presented in Fig. 2c–f. The EDS mappings reveal that Cu and Mg elements are uniformly distributed across the Al matrix. Some Cu-rich micro dots are observed, corresponding to the Cu-rich precipitates. TEM characterizations on the CNT/2024Al composite are presented in Fig. 2g–j, including the elongated Al grains in the ED-ND plane (Fig. 2g), the structural integrity of CNTs (Fig. 2h and i), the rod-shaped Al_4C_3 phase (Fig. 2i) and the Al–Al_4C_3 interface (Fig. 2j). The interplane spacing of the (012) plane and (003) plane of the Al_4C_3 phase is about 0.28 nm and 0.83 nm, respectively [14,21].

Fig. 3a–c present the SEM micrographs of the as-received CNT/2024Al after electrolysis. The white patches (Fig. 3a) and stripes (Fig. 3b and c) are oxygen-rich according to EDS maps (inset in Fig. 3b), and are supposed to be oxidates formed during electrolysis [43]. The particle – particle interfaces are less resistant to electrolysis than particle interiors [44] and holes and pits may form in

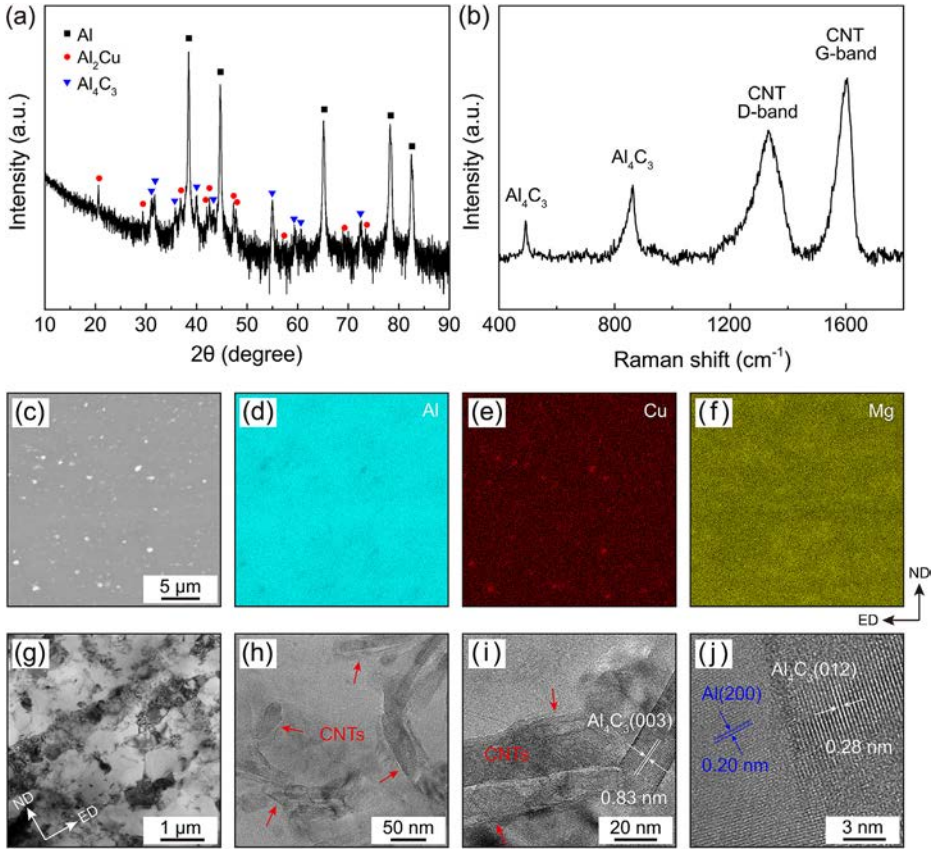

Fig. 2. Composition and microstructural characterizations of the as-received CNT/2024Al composite. (a) XRD. (b) Raman spectroscopy. (c) Backscattered electron image, and (d)–(f) EDS distribution maps of Al, Cu and Mg. (g) TEM image of the Al matrix grains, and HR-TEM images of (h) CNTs, (i) CNTs and Al_4C_3, and (j) the Al–Al_4C_3 interface. (A colour version of this figure can be viewed online.)

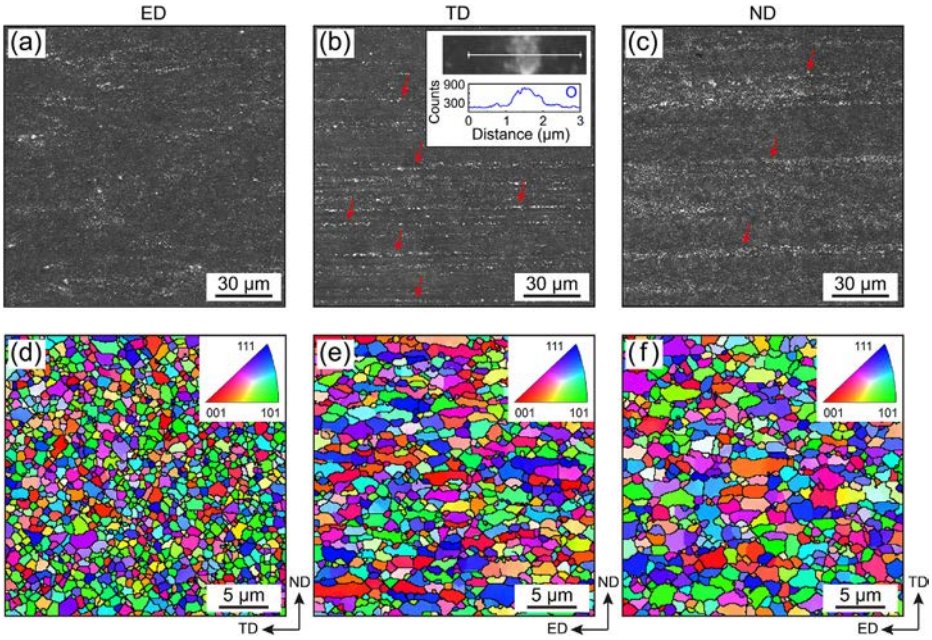

Fig. 3. (a)–(c) SEM micrographs of the as-received CNT/2024Al composite after electrolysis. Inset of b: oxygen abundance distribution in a line across a white patch. (d)–(f) EBSD characterization (inverse pole figure maps) of the as-received CNT/2024Al composite. (A colour version of this figure can be viewed online.)

the interface areas, which facilitates concentration of oxidates there. Therefore, the white regions can be used to mark the morphology of the lamellar microstructures. The lamellar microstructures are aligned lengthwise along the ED, and exhibit a smaller spacing in the ED-TD plane (~8 μm) than that in the ED-ND plane (~28 μm), consistent with the extrusion geometry (Fig. 1b). In addition, such lamellar microstructures were observed in other extruded materials [45,46]. The EBSD inverse pole figure maps (Fig. 3d–f) show elongated grains along the ED in the ED-TD and ED-ND planes, and grains are approximately equiaxial in the TD-ND plane. Grain orientations in the three planes are similar. The average grain sizes are 0.77±0.29 μm, 1.02±0.49 μm and 1.02±0.51 μm in the TD-ND, ED-ND and ED-TD planes, respectively.

2.3. Plate impact experiments

Plate impact experiments are conducted on single-stage gas guns with a 14-mm or 28-mm bore diameter. Fig. 4a presents a schematic configuration of the plate impact experiments. A flyer plate (4) is attached to the front end of an aluminum sabot (2), with a recess (5) behind it. To prevent gas leakage, two O-rings (3) are fixed to the aluminum sabot. When a solenoid valve is fired, high pressure gas (helium or nitrogen) stored in a reservoir is released into the gun barrel (1) to accelerate the sabot and flyer plate system which impacts the CNT/2024Al composite target (7). The flyer plate velocity or impact velocity (u_{imp}) is measured with an optical beam block system (6) as the flyer plate exits the muzzle. A Doppler pin system (DPS) (12) is adopted to capture the free surface velocity (u_{fs}) history of the target. Optical signals are analyzed to derive velocity histories via sliding window fast Fourier transformation. The muzzle, target, DPS and related optics are located in a vacuum chamber (14). For microstructure characterizations, the impacted targets are "soft-recovered" with soft materials (13). The uncertainties in flyer plate velocity and free surface velocity measurements are less than 1%.

The flyer plates are made of 6061 aluminum alloy with $\rho_0 = 2.73\pm0.01$ g cm^{-3}, $C_L = 6407\pm31$ m s^{-1}, and $C_B = 5272\pm 68$ m s^{-1}. Flyer plates and samples are of a disk shape with a diameter of 13.20±0.01 mm and 9.00±0.01 mm, respectively. The nominal thicknesses of the flyer plates and targets are fixed at 1.00±0.01 mm and 2.00±0.01 mm, respectively.

The samples are shock-loaded along the ED, TD and ND to investigate the effects of microstructural anisotropy. Disk-shaped samples with different orientations are harvested using electrical discharge machining. Sample preparation scheme and loading directions (blue arrows) are illustrated in Fig. 4b. Plate impact experiments are achieved at low (~240 m s^{-1}) and high (~330 m s^{-1}) impact velocities, respectively.

Postmortem samples are characterized with XCT and SEM. The spatial distribution of cracks in a spallation region is obtained with XCT. XCT experiments are performed at beamline BL13W1 of the Shanghai Synchrotron Radiation Facility with a nominal resolution of 0.65 μm. Details of XCT characterization can be found elsewhere [47].

3. Results and discussions

3.1. Free surface velocity analysis

Impact experiments are performed at two impact velocities along three orientations (ED, TD and ND). The free velocity time series are presented in Fig. 5, and the experimental parameters are listed in Table 1. The free-surface velocity time series, $u_{fs}(t)$, show different damage features at low and high impact velocities.

The sample free surface velocity profile (Fig. 5) labelled with *A–G* illustrates the compression-tension process during plate impact experiments, including dynamic compression, ensuing release, and spallation. Segment *AB* denotes the elastic precursor, and *B*, the HEL. The plastic wave *BC* follows the elastic precursor and develops into a supported, stable shock *CD*. When the release fan, which is reflected by the flyer plate back surface, arrives at the target free surface, the free-surface velocity of target drops (*DE*; release). The interaction of this release fan with that initiated from the free surface of the target induces tension in the target interior. If

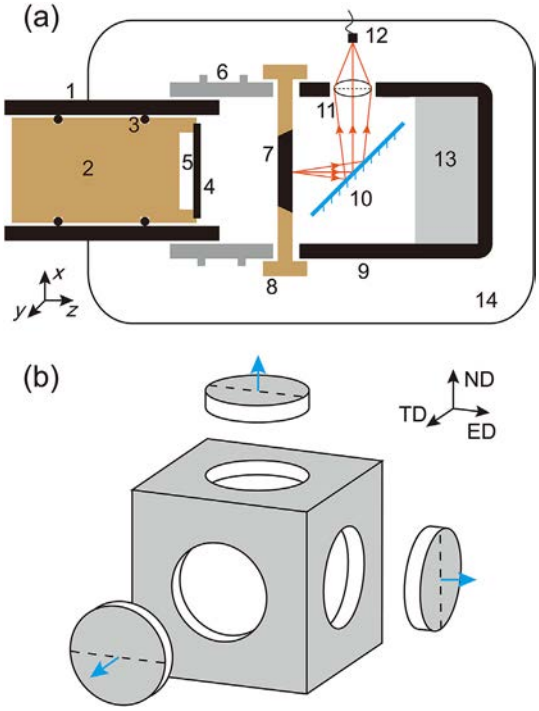

Fig. 4. (a) Schematic setup for plate impact experiments. 1: gun barrel; 2: aluminum alloy sabot; 3: O-ring; 4: flyer plate; 5: recess for release waves; 6: optical fibers connected to the detectors for the optical beam block system; 7: sample; 8: sample holder; 9: recovery cylinder; 10: turning mirror; 11: lens; 12: optical fiber connected to the Doppler pin system (DPS); 13: soft materials; 14: vacuum chamber. (b) Illustration of the loading axis with respect to the sample coordinate system (ED-TD-ND), and the scheme for harvesting specimens. Dashed lines represent cutting planes for microstructural characterization. (A colour version of this figure can be viewed online.)

the tensile stress exceeds the dynamic tensile or spall strength of the target, spallation occurs. At the segments *EF* and *FG*, the velocity increases, due to arrival of the compression wave which stems from the spall plane within the material. The re-acceleration starting at *E* is the typical spall mark. The slope of *EF* is attributed to independent growth of isolated voids or cracks, and *FG*, to their coalescence [48,49].

Various mechanical parameters such as HEL, von Mises yield stress (σ_y), peak stress (σ_H), strain rate ($\dot{\varepsilon}$), re-acceleration (a_r) and spall strength (σ_{sp}) can be deduced from free surface velocity profiles, $u_{fs}(t)$. In particular, the spall strength is calculated from the pullback velocity with the acoustic method as [26,50].

$$\sigma_{sp} \approx \frac{1}{1+\frac{C_L}{C_B}} \rho_0 C_L \Delta u, \tag{1}$$

where the pullback velocity $\Delta u = u_{fs,D} - u_{fs,E}$. Definition and calculation of the other parameters listed above have been detailed in previous studies [49–55] and will not be repeated here.

The mechanical parameters of the CNT/2024Al composite under plate impact are summarized in Table 1. The HEL, corresponding to the yield point at the one-dimensional strain state, ranges from 0.75 to 0.85 GPa while $\sigma_y$from 0.38 to 0.43 GPa. The HEL and σ_y changes little with different sample orientations and impact velocities. Anisotropy on HEL and σ_y can essentially be neglected. The strain rates varies from 1.22×10^5 s^{-1} to 1.64×10^5 s^{-1}, and increase monotonously with increasing peak stress for three orientations. The spall strengths of the CNT/2024Al composite range from 1.4 to 1.9 GPa. The spall strengths along the ED are ~50% higher than that of the commercial 2024Al alloys at similar impact velocities (1.7–1.9 GPa at 240 – 330 m s^{-1} versus 1.1 – 1.4 GPa at 180 – 560 m s^{-1} [56]).

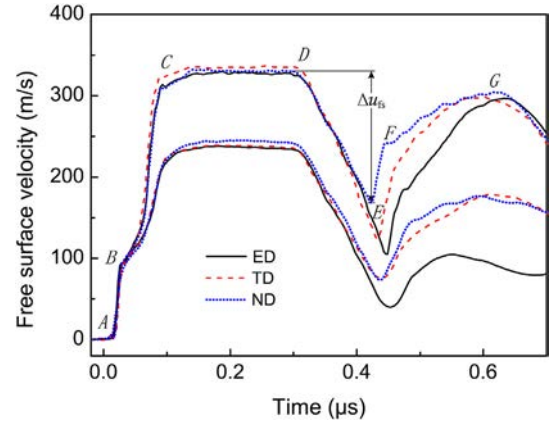

Fig. 5. Representative free-surface velocity–time curves, $u_{fs}(t)$, for impact loading along the ED (black solid curves), TD (red dashed curves) and ND (blue doted curves). (A colour version of this figure can be viewed online.)

3.2. XCT characterization of postmortem samples

For three low impact velocity shots (u_{imp} ~240 m s^{-1}), the postmortem samples are characterized with synchrotron XCT. Their spatial distributions of microcracks are presented in Fig. 6a–c, each within a sampling volume of 640 × 640 × 850 μm^3, and demonstrate a damage anisotropy as a result of the microstructural anisotropy. During spallation, microcracks nucleate preferentially between layers and propagate along a preferred direction. For ED (Fig. 6a), there are merely some discrete microcracks, while macrocracks appear for the other two loading directions (Fig. 6b and c). Therefore, under the same loading condition, the ED-loading has higher spallation resistance, consistent with the spall strength (free surface velocity) measurements in Fig. 5.

The loading along the TD and ND (Fig. 6b and c) induces higher damage degree: there is a predominant crack at the center, as a result of nucleation, growth and coalescence of microcracks. In addition, the main crack in Fig. 6c is more straight than that in Fig. 6b (marked by red dashed arrows), indicating collinear propagation of the initial cracks for ND-loading with the least resistance due to lamellar microstructures are mostly perpendicular to ND. Consistently, the slope *EF* (spall-induced re-acceleration) is the steepest as seen in its free surface velocity history (Fig. 5).

For the TD- and ND-loading, cracks extend on the ED-ND and ED-TD plane, respectively, perpendicular to the loading directions. For the ED-loading, cracks are parallel to ED-TD planes, and connected by the cracks on the ED-ND plane, showing a stairway shape (Fig. 6d). For all these three loading cases, the propagation direction of microcracks is along the ED, regardless of the loading direction. However, the loading direction has significant effect on damage degree, which is attributed to the microstructural anisotropy. As seen from Fig. 6d–f (magnified views of Fig. 6a–c), crack surface roughness decreases in the following order: ED > TD > ND, and is closely related to the degree of collinear propagation of microcracks, which is in turn a result of microstructural anisotropy and loading direction.

From 3D crack configurations obtained with XCT, crack volume distribution can be characterized in terms of the normalized crack number $\overline{N}_c(k)$, using the binning procedure described in Ref. [57].

Table 1
Experimental parameters. L_f: flyer plate thickness; L_s: sample thickness; u_{imp}: impact velocity; σ_{HEL}: Hugoniot elastic limit; σ_y: von Mises yield stress; σ_H: peak stress; $\dot{\varepsilon}$: tensile strain rate; σ_{sp}: spall strength; a_r: re-acceleration. Numbers in parentheses denote uncertainties in the last one or two digits.

Orientation	L_f (mm)	L_s (mm)	u_{imp} (m s^{-1})	σ_{HEL} (GPa)	σ_y (GPa)	σ_H (GPa)	$\dot{\varepsilon}$ (× 10^5 s^{-1})	σ_{sp} (GPa)	a_r (× 10^9 m s^{-2})
ED	1.01 (1)	1.99 (1)	238 (3)	0.84 (2)	0.43 (4)	2.53 (6)	1.36 (2)	1.66 (4)	1.30 (15)
TD	1.01 (1)	2.00 (1)	239 (3)	0.77 (3)	0.39 (5)	2.54 (6)	1.22 (3)	1.39 (3)	1.45 (14)
ND	1.01 (1)	2.00 (1)	244 (3)	0.75 (3)	0.38 (6)	2.58 (8)	1.27 (3)	1.41 (3)	1.69 (9)
ED	1.00 (1)	2.00 (1)	329 (4)	0.85 (2)	0.43 (4)	3.48 (4)	1.52 (1)	1.88 (5)	3.17 (12)
TD	1.00 (1)	1.99 (1)	335 (4)	0.85 (2)	0.43 (4)	3.54 (5)	1.64 (2)	1.77 (5)	3.61 (7)
ND	1.00 (1)	2.01 (1)	332 (4)	0.85 (3)	0.43 (5)	3.51 (5)	1.32 (2)	1.42 (3)	3.90 (11)

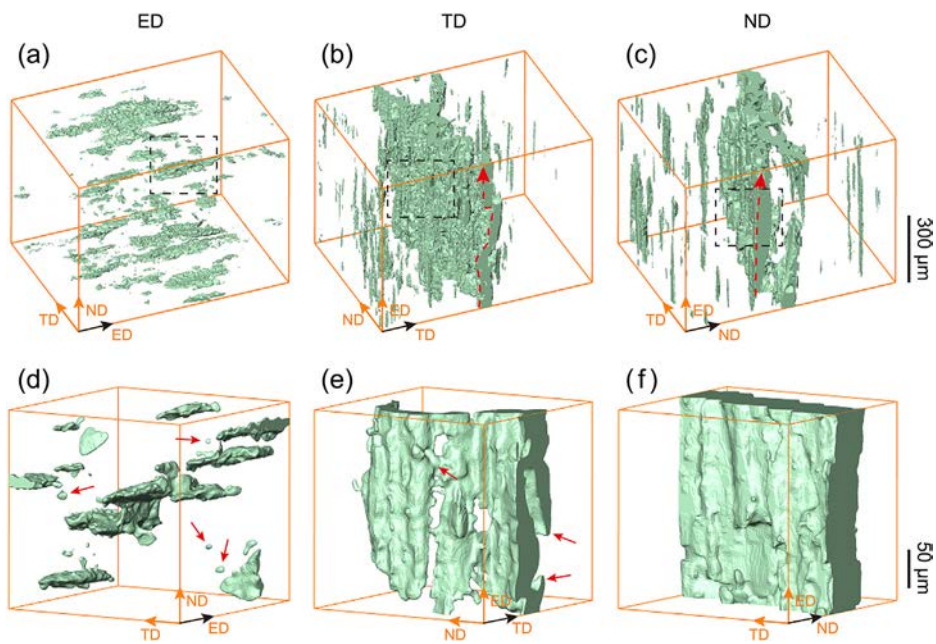

Fig. 6. (a)–(c) X-ray computed tomography images of the postmortem samples impacted along the ED, TD and ND. (d)–(f) Magnified views corresponding to the regions indicated by the rectangles with black dashed lines in (a)–(c). Only cracks are shown in green. Impact velocity: ~240 m s^{-1}. (A colour version of this figure can be viewed online.)

$$\overline{N}_c(k) = \frac{1}{\lambda^k} \sum_{\lambda^{k-1} \le V_c \le \lambda^k - 1} N_c(V_c), \tag{2}$$

where $N_c(V_c)$ is the number of cracks with volume V_c located in a volume (in μm^3) bin (λ^{k-1}, λ^k-1), and k (integers) denotes the sequence number of bins. λ is a constant (1.78 here) and can be used to control the bin width. $\overline{N}_c(k)$ obtained for different orientations is presented in Fig. 7a. The crack volume distributions for three loading directions are approximately consistent, irrespective of their different crack morphologies (Fig. 6a–c). They can be described with the same power-law function, i.e. $\overline{N}_c \propto V_c^{-1.4}$, indicating similar nucleation and growth dynamics in three loading directions [58].

The topology of crack networks can be characterized via gyration tensor analyses [34,35]. A gyration tensor is defined in terms of the 3D voxel coordinate data of a crack. Then the eigenvectors and eigenvalues of the gyration tensor are calculated, and the eigenvalues are denoted as R_1, R_2 and R_3 ($R_1 > R_2 > R_3$). After that, a characteristic ellipsoid can be constructed for the crack with three semi-axes oriented along the eigenvectors, and their lengths as $a = \sqrt{5R_1}$, $b = \sqrt{5R_2}$ and $c = \sqrt{5R_3}$, respectively. Using the eigenvalues, a sphericity index can be defined as

$$S_G = 1 - \frac{1}{2} \frac{\sum_{i>j}^{3} (R_i - R_j)^2}{\left(\sum_i^3 R_i\right)^2}, \tag{3}$$

where i, j = 1, 2, 3. Two aspect ratios, elongation index (EI) and flatness index (FI), can be calculated as

$$\mathrm{EI} = b/a, \text{and } \mathrm{FI} = c/b. \tag{4}$$

A smaller EI or FI value means a greater degree of elongation or flatness.

The sphericity distributions of cracks for the three types of samples are presented in Fig. 7b. The sphericity of cracks for ED-loading varies mainly in the range of 0.65 – 0.95, and its mean sphericity (0.67) is considerably higher than those for TD- and ND-loading (~0.40). Sphericity of cracks is similar for TD- and ND-loading. The cracks for ED-loading are statistically more spherical than those for TD- and ND-loading, consistent with Fig. 6d (red arrows), because the growth and coalescence of microcraks are blocked by particle interfaces in the ED-TD and ED-ND planes for ED-loading. The EI distributions of cracks for TD- and ND-loading are similar and concentrate in the small-EI region (Fig. 7c). The mean EI values for TD- and ND-loading (~0.20) are much smaller than that for ED-loading (0.40). The reason is that cracks for TD- and ND-loading are largely elongated in the ED along which the lamellar microstructures are aligned lengthwise and thus cracks

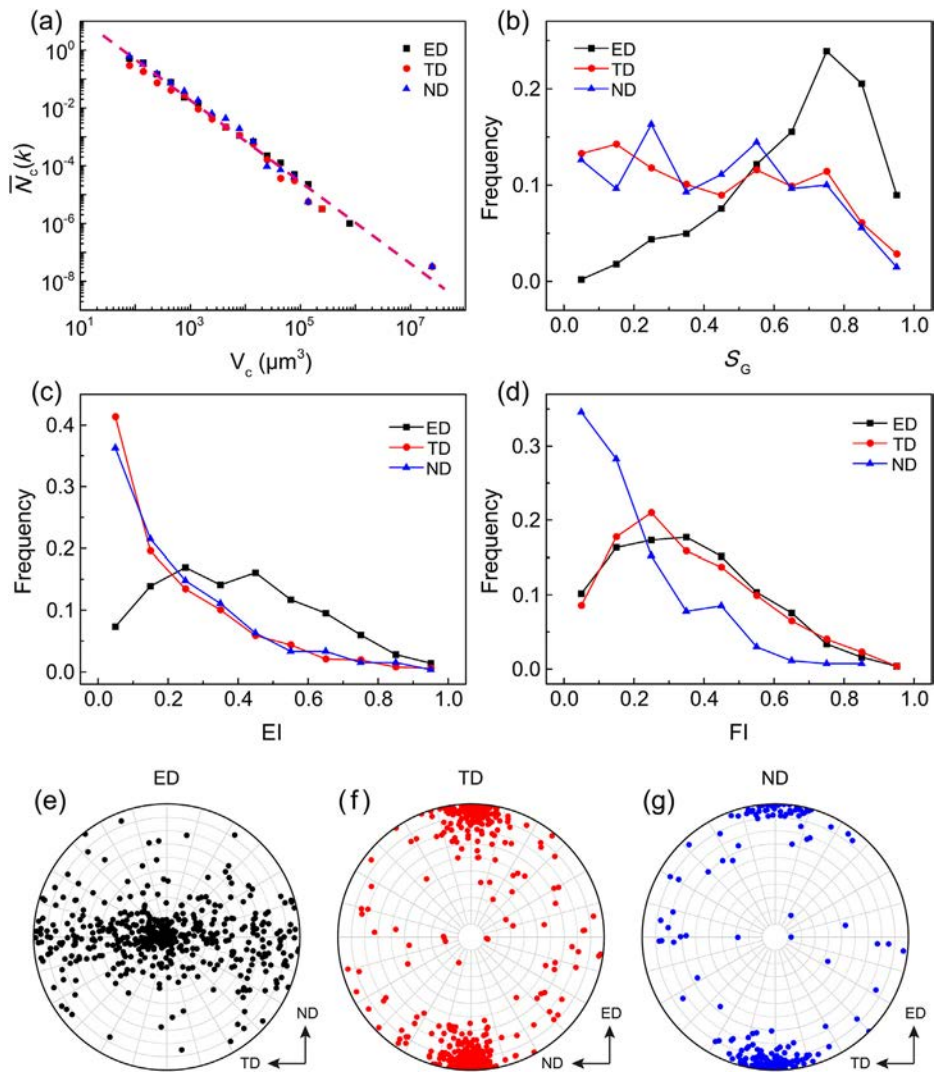

Fig. 7. Characterizations on the topology of crack networks in three types of samples. (a) Number–volume distribution of cracks. The dashed line is a power fitting to the experimental data. (b)–(d) Sphericity index (S_G), elongation index (EI) and flatness index (FI) distributions of cracks, respectively. (e)–(g) Pole figures of the longest principal axis of cracks. Impact velocity: ~240 m s^{-1}. (A colour version of this figure can be viewed online.)

are more likely to propagate. It is interesting to note that the FI distribution of cracks for ND-loading is different from that for TD-loading (Fig. 7d), although they both exhibit elongated cracks in the ED. The mean FI for ND-loading (0.20) is appreciably smaller than those for TD-loading (0.35), indicating that the cracks for ND-loading are flatter and own fewer branches, in contrast with TD-loading in Fig. 6e (branches are marked by red arrows), due to a large amount of microcracks propagating collinearly.

A method similar to stereographic projection is used to project microcrack orientations into a pole figure. Firstly, a coordinate system (*O-xyz*) is established, and a sphere centered at the origin is constructed. One endpoint of the longest axis (*a*) is set at the origin *O* and the other endpoint is extended to intersect the sphere at *L*. The line connecting point *L* and a pole intersects the equatorial plane (the *xy*-plane) at point *M*, which indicates the orientation of the microcrack. The angle between the longest axis and the *z*-axis is measured as θ, which is called the angle of pitch. The angle between the projection of the longest axis onto the equatorial plane and the *x*-axis is measured as φ, which is called the direction angle.

All microcrack orientations for the three loading directions in Fig. 6a–c are plotted in their corresponding pole figures (Fig. 7e–g). For the ED-loading (Fig. 7e), most of the cracks are oriented along the ED, while a few are oriented along the TD. For loading along the TD and ND (Fig. 7f and g), the majority of the microcracks are along the ED, while only a few are along the TD and ND. For the ND-loading, the extent of crack propagation along the ED is significantly greater than the TD-loading. This is because the lamellar microstructures of the composite are elongated along the ED and mostly perpendicular to the ND. It is of the least resistance for cracks to propagate between layers, forming microcracks that extend parallel to the ED-TD plane and along the ED. A small number of microcracks parallel to the ED-ND plane can form, since some loading directions are not completely perpendicular to the lamellar microstructures, and the microcrack propagation connection is relatively difficult.

The numbers of cracks in the ED, TD and ND samples shown in Fig. 6a–c are 502, 527 and 270, respectively, and the corresponding crack volumes are 0.29×10^7 μm^3, 1.93×10^7 μm^3 and 2.23×10^7 μm^3 (Table 2). In the ND sample, the loading direction is perpendicular to most lamellar microstructures (the ED-TD plane), and the cracks are more prone to collinear propagation and coalescence. Although the number of cracks is the least, the crack volume is the largest. In

the TD sample, the degree of collinear propagation is lower than that in the ND sample, resulting in a smaller crack volume and a larger number of microcracks. In the ED sample, the loading direction is parallel to the long axis of the lamellar microstructures, microcrack propagation is the most difficult, and the energy is mainly consumed in the crack nucleation stage.

The degree of damage $\mathscr{D}(z)$ is defined as

$$\mathscr{D}(z) = \frac{S_c(z)}{S_t(z)}, \tag{5}$$

where $S_c(z)$ and $S_t(z)$ are damage area and total area observed in the z-slice of XCT, respectively. Fig. 8 shows the damage distribution (degree of damage vs distance from free surface) along these three loading directions. Main damage occurs in the range of 800–1200 μm. The damage peak values of the TD and ND samples are similar ($\mathscr{D} \sim 0.39$) and appear at similar distances (1000 μm). However for the ND sample, its main peak is flanked by two small peaks ($\mathscr{D} \sim 0.15$ and 0.21). This is because the microcracks in the ND sample are prone to collinear expansion, forming multiple large cracks within a certain range. For ED sample, the damage peak value is merely 0.03, much smaller than those of TD and ND samples, and the peak location is not in the centre of the sample. This is because the impact direction is parallel to the long axis of lamellar microstructures, and the coalescence of microcracks is hindered; only a very small number of cracks are connected.

3.3. SEM characterization of postmortem samples

The postmortem samples for higher impact velocities (~330 m s^{-1}) are characterized with SEM (Fig. 9). The samples are also sectioned along the dashed line in Fig. 4b. The fractographs of the fracture surfaces are shown in Fig. 9a–c for the ED, TD and ND samples, respectively. The corresponding main crack lengths are 6.1 mm, 7.4 mm and 8.7 mm, and the maximum widths of the respective main cracks are 133 μm, 228 μm and 379 μm. In addition, the crack width of the ED sample is 645 μm if we include the microcracks extending along the impact direction, much larger than those for the TD and ND samples. This difference is again due to the microstructural anisotropy of the CNT/2024Al composite.

Fig. 9d–f are magnified views of the central spallation regions delimited by the dashed rectangles in Fig. 9a–c, respectively. For similar impact velocities (~330 m s^{-1}), the damage degree along the ED is less than those along the TD and ND, and the damage evolution shows strong anisotropy. For ED, the main crack is serrated, and there are many microcracks parallel to the impact direction. For both TD and ND samples, cracks are perpendicular to the impact direction. Because most lamellar microstructures are perpendicular to the ND, the composite is most vulnerable to damage when impacted along the ND. Fig. 9f shows striated traces on the crack surface for ND, while they are absent for TD (Fig. 9e). Fig. 9e shows that a band structure in the crack connects the upper and lower crack surfaces. Collinear crack expansion is more difficult for TD-loading than ND-loading. These differences are also reflected in the free surface velocity histories (Fig. 5).

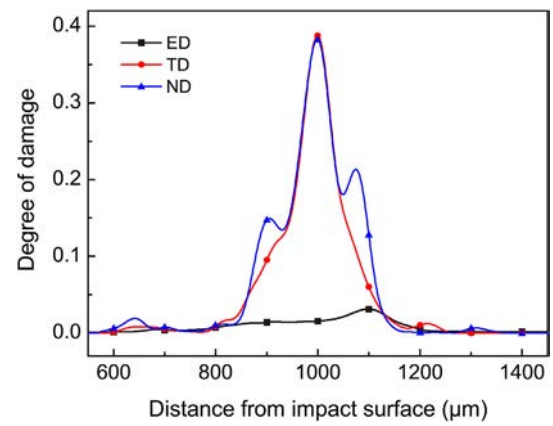

Fig. 8. Degree of damage as a function of distance away from the impact surface for three different impact directions (ED, TD and ND). Impact velocity: ~240 m s^{-1}. (A colour version of this figure can be viewed online.)

SEM fractographs of postmortem samples (Fig. 10) are used to analyze further the mechanism of spallation in the CNT/2024Al composite for three different loading directions. The large cracks extend along the ED with a stairway shape (marked by red arrows in Fig. 10a), corresponding to the cracks extending along the impact direction in Fig. 9a and d. For the TD- and ND-loading (Fig. 10b and c), the fracture surfaces show horizontal striations, but more interface debonding is observed for the ND-loading. The fracture surfaces are rougher for the TD-loading (Fig. 10b) than those for the ND-loading (marked by red arrows in Fig. 10c), as a result of the weak bonding at particle interfaces for the ND-loading (Fig. 5). High-magnification fractographs are shown in Fig. 10d–f. CNTs (marked by red arrows) are exposed on the fracture surfaces, and the exposed length is far less than 1 μm. Therefore, CNTs are fractured after a small amount of sliding (Fig. 10d–f) under plate impact loading [59], which indicates the existence of bridged CNTs linking the particles due to some rotation of CNTs during hot extrusion. In contrast, CNTs in AMCs are pulled out longer from the Al matrix, and microvoids (dimples) are formed around these CNTs under quasi-static tension [60].

Previous studies [28,29,31] reported that the spall strengths of AMCs were reduced by the addition of Al_2O_3 filaments/particles. In our case, CNTs appear to enhance the spall strength of the 2024Al matrix compared to the commercial 2024Al alloy [56]. Several mechanisms can be responsible for this strengthening effect of CNTs. First and foremost, the load transfer from matrix to CNTs and the strong CNT/matrix bonding due to the formation of nanoscale Al_4C_3 domains at the CNT/matrix interfaces [7,61] can improve the fracture strength of CNT-reinforced AMCs. Such mechanisms have been extensively discussed under quasi-static loading [14,16,17,62], and are also applicable to dynamic loading where the bridged CNTs promote the interfacial tensile strengths of Al–Cu–Mg particles and thus the spall strength of CNT/2024Al. In addition, the rough surfaces of particles coated with CNTs increase the interface friction between particles and can raise the spall strength of CNT/2024Al as

Table 2
Characteristic parameters of cracks in three samples impacted at ~240 m s^{-1} along the ED, ND, and TD. The sampling volume is 850 × 640 × 640 μm^3. n: number of cracks; V_{total}: total crack volume; V_{max}: maximum volume of individual cracks; $\overline{V}$: average volume of cracks; $\overline{D}$: average diameter of cracks; S_G: sphericity; EI: elongation index; FI: flatness index. Numbers in parentheses denote uncertainties in the last one or two digits, and standard deviations with asterisks.

Orientation	n	V_{total} (×10^7 μm^3)	V_{max} (×10^7 μm^3)	$\overline{V}$(×10^4 μm^3)	$\overline{D}$ (μm)	S_G	EI	FI
ED	502	0.29 (2)	0.08 (1)	0.57 (5)	22 (1)	0.67 (0.20*)	0.40 (0.22*)	0.35 (0.20*)
TD	527	1.93 (7)	1.80 (7)	3.66 (14)	41 (1)	0.43 (0.27*)	0.21 (0.20*)	0.35 (0.20*)
ND	270	2.23 (8)	2.12 (8)	8.25 (31)	54 (1)	0.42 (0.25*)	0.22 (0.20*)	0.20 (0.16*)

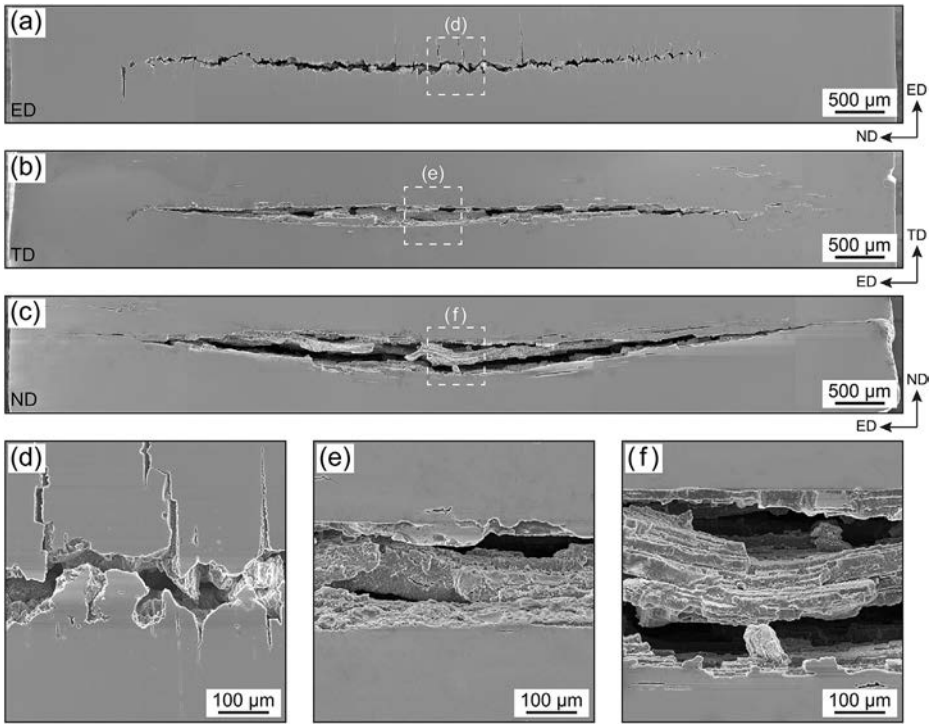

Fig9. SEM micrographs of sectioned postmortem samples for impact loading along (a) ED, (b) TD and (c) ND. (d)–(f) Magnified views corresponding to the regions indicated by the rectangles in (a)–(c). Impact velocity: ~330 m s^{-1}.

well. The pinning effect of CNTs generally leads to grain refinement in CNT-reinforced AMCs [17], and leads to an increase in their fracture strengths under quasi-static loading. However, the grain size, in the range of several to hundreds of microns, shows little influence on the spall strength of materials under impact loading [63].

4. Summary

The CNT/2024Al composite fabricated by flake powder metallurgy and hot extrusion is subjected to plate impact loading along three different directions (ED, ND, and TD) at two representative (low and high) impact velocities. Our main conclusions are:

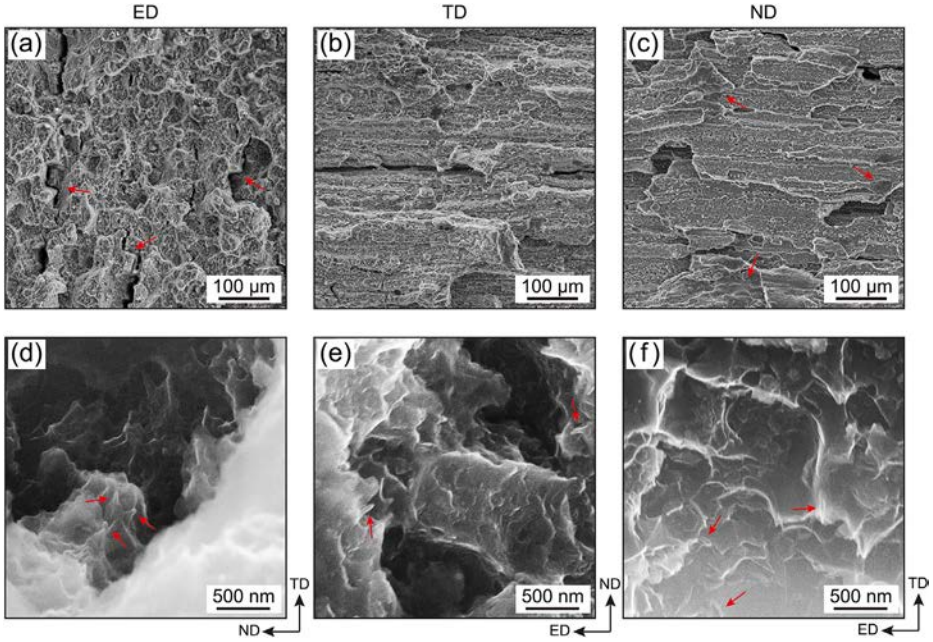

Fig. 10. SEM fractographs of shock-recovered samples for impact loading along the ED, TD and ND, at two different magnifications. Impact velocity: ~330 m s^{-1}. (A colour version of this figure can be viewed online.)

- The microstructural anisotropy (in terms of orientations of the lamellar microstructures) of the CNT/2024Al composite has a negligible effect on HEL (~0.8 GPa) but induces an anisotropy in spall strength (1.4 – 1.9 GPa) at different impact velocities. Spall strength is the highest for loading along the ED, the long axis of the lamellar microstructures.
- CNTs appear to increase the spall strength of the 2024Al alloy, in contrast to other (e.g. Al_2O_3) reinforcing fibers/particles.
- The crack volume distributions for three loading directions are approximately consistent, following the same power-law function. However, the cracks for ED-loading are statistically more spherical than those for TD- and ND-loading, because the growth and coalescence of microcraks are blocked by particle interfaces in the ED-TD and ED-ND planes, resulting the highest spall strength.
- Propagation of microcracks is along the ED regardless of the loading direction. Damage degree decreases in the order of ND > TD > ED, because of the easier propagation of cracks along the ED for the TD- and ND-loading. However, the cracks for the ND-loading are flatter and have fewer branches, due to a large amount of microcracks propagating collinearly, corresponding to the maximum damage degree.

Credit authorship contribution statement

J. C. Cheng: Conceptualization, Methodology, Investigation, Visualization, Data curation, Writing -original draft. **H. W. Chai:** Methodology,Visualization. **G. L. Fan:** Resources. **Z. Q. Li:** Resources. **H. L. Xie:** Resources. **Z. Q. Tan:** Resources, Visualization. **B. X. Bie:** Supervision, Modify -original draft. **J.Y. Huang:** Validation, Supervision, Modify -original draft. **S. N. Luo:** Writing -review \& editing, Validation, Supervision, Funding acquisition, Resources.

Declaration of competing interest

The authors declare that they have no known competing financial interests or personal relationships that could have appeared to influence the work reported in this paper.

Acknowledgments

The XCT measurements were conducted at beamline BL13W1 of Shanghai Synchrotron Radiation Facility. This work was supported by National Natural Science Foundation of China (Grant Nos. 11627901 and 11802252) and the Science and Technology Program of Sichuan Province (Grant No. 2020YFG0415).

References

[1] Y.N. Xia, P.D. Yang, Y.G. Sun, Y.Y. Wu, B. Mayers, B. Gates, Y.D. Yin, F. Kim, H.Q. Yan, One-dimensional nanostructures: synthesis, characterization, and applications, Adv. Mater. 15 (5) (2003) 353–389.
[2] M.S. Dresselhaus, G. Dresselhaus, R. Saito, Physics of carbon nanotubes, Carbon 33 (7) (1995) 883–891.
[3] R.S. Ruoff, D.C. Lorents, Mechanical and thermal properties of carbon nanotubes, Carbon 33 (7) (1995) 925–930.
[4] S. Riichiro, G. Dresselhaus, M.S. Dresselhaus, Physical Properties of Carbon Nanotubes, Imperial College Press, London, 1998.
[5] P.R. Bandaru, Electrical properties and applications of carbon nanotube structures, J. Nanosci. Nanotechnol. 7 (4–5) (2007) 1239–1267.
[6] P.J.F. Harris, P.J.F. Harris, Carbon Nanotube Science: Synthesis, Properties and Applications, Cambridge Univ. Press, Cambridge, 2009.
[7] H. Kwon, M. Estili, K. Takagi, T. Miyazaki, A. Kawasaki, Combination of hot extrusion and spark plasma sintering for producing carbon nanotube reinforced aluminum matrix composites, Carbon 47 (3) (2009) 570–577.
[8] W. Zhou, S. Bang, H. Kurita, T. Miyazaki, Y. Fan, A. Kawasaki, Interface and interfacial reactions in multi-walled carbon nanotube-reinforced aluminum matrix composites, Carbon 96 (2016) 919–928.
[9] K.M. Yang, X.D. Yang, E.Z. Liu, C.S. Shi, L.Y. Ma, C.N. He, Q.Y. Li, J.J. Li, N.Q. Zhao, High strain rate dynamic compressive properties and deformation behavior of Al matrix composite foams reinforced by in-situ grown carbon nanotubes, Mater. Sci. Eng. A 729 (2018) 487–495.
[10] J.A. Reglero, M.A. Rodriguez-Perez, E. Solorzano, J.A. De Saja, Aluminium foams as a filler for leading edges: improvements in the mechanical behaviour under bird strike impact tests, Mater. Des. 32 (2) (2011) 907–910.
[11] M.E. Melis, J.H. Brand, J.M. Pereira, D.M. Revilock, Reinforced Carbon-Carbon Subcomponent Flat Plate Impact Testing for Space Shuttle Orbiter Return to Flight, 2007, pp. 1–16. NASA/TM-2007-214384.
[12] M. Jafari, M.H. Abbasi, M.H. Enayati, F. Karimzadeh, Mechanical properties of nanostructured Al2024–MWCNT composite prepared by optimized mechanical milling and hot pressing methods, Adv. Powder Technol. 23 (2) (2012) 205–210.
[13] G.L. Fan, Y. Jiang, Z.Q. Tan, Q. Guo, D.B. Xiong, Y.S. Su, R.B. Lin, L. Hu, Z.Q. Li, D. Zhang, Enhanced interfacial bonding and mechanical properties in CNT/Al composites fabricated by flake powder metallurgy, Carbon 130 (2018) 333–339.
[14] B. Chen, J. Shen, X. Ye, H. Imai, J. Umeda, M. Takahashi, K. Kondoh, Solid-state interfacial reaction and load transfer efficiency in carbon nanotubes (CNTs)-reinforced aluminum matrix composites, Carbon 114 (2017) 198–208.
[15] A.M.K. Esawi, K. Morsi, A. Sayed, M. Taher, S. Lanka, Effect of carbon nanotube (CNT) content on the mechanical properties of CNT-reinforced aluminium composites, Compos. Sci. Technol. 70 (16) (2010) 2237–2241.
[16] F. Mokdad, D.L. Chen, Z.Y. Liu, B.L. Xiao, D.R. Ni, Z.Y. Ma, Deformation and strengthening mechanisms of a carbon nanotube reinforced aluminum composite, Carbon 104 (2016) 64–77.
[17] D.H. Nam, S.I. Cha, B.K. Lim, H.M. Park, D.S. Han, S.H. Hong, Synergistic strengthening by load transfer mechanism and grain refinement of CNT/Al-Cu composites, Carbon 50 (7) (2012) 2417–2423.
[18] L. Jiang, Z.Q. Li, G.L. Fan, L.L. Cao, D. Zhang, The use of flake powder metallurgy to produce carbon nanotube (CNT)/aluminum composites with a homogenous CNT distribution, Carbon 50 (5) (2012) 1993–1998.
[19] R. Xu, Z.Q. Tan, D.B. Xiong, G.L. Fan, Q. Guo, J. Zhang, Y.S. Su, Z.Q. Li, D. Zhang, Balanced strength and ductility in CNT/Al composites achieved by flake powder metallurgy via shift–speed ball milling, Compos. Appl. Sci. Manuf. 96 (2017) 57–66.
[20] R. Xu, Z.Q. Tan, G.L. Fan, G. Ji, D.B. Xiong, Q. Guo, Y.S. Su, Z.Q. Li, D. Zhang, High-strength CNT/Al-Zn-Mg-Cu composites with improved ductility achieved by flake powder metallurgy via elemental alloying, Compos. Appl. Sci. Manuf. 111 (2018) 1–11.
[21] M.L. Chen, G.L. Fan, Z.Q. Tan, D.B. Xiong, Q. Guo, Y.S. Su, J. Zhang, Z.Q. Li, M. Naito, D. Zhang, Design of an efficient flake powder metallurgy route to fabricate CNT/6061Al composites, Mater. Des. 142 (2018) 288–296.
[22] M. Unosson, L. Nilsson, Projectile penetration and perforation of high performance concrete: experimental results and macroscopic modelling, Int. J. Impact Eng. 32 (7) (2006) 1068–1085.
[23] G. Corderley, F. Mostert, J. Krüger, Failure modes in a carbon/titanium fibre metal laminate under hyper-velocity impact, Int. J. Impact Eng. 125 (2019) 180–187.
[24] M. Altenaiji, Z.W. Guan, W.J. Cantwell, Y. Zhao, G.K. Schleyer, Characterisation of aluminium matrix syntactic foams under drop weight impact, Mater. Des. 59 (2014) 296–302.
[25] H. Huh, W.J. Kang, S.S. Han, A tension split Hopkinson bar for investigating the dynamic behavior of sheet metals, Exp. Mech. 42 (1) (2002) 8–17.
[26] T. Antoun, D.R. Curran, L. Seaman, G.I. Kanel, S.V. Razorenov, A.V. Utkin, Spall Fracture, Springer Science, New York, 2003.
[27] D.M. Schuster, R.P. Reed, Fracture behavior of shock-loaded boron-aluminum composite materials, J. Compos. Mater. 3 (3) (1969) 562–576.
[28] R.S. Hixson, J.N. Johnson, G.T. Gray III, J.D. Price, Effects of interfacial bonding on spallation in metal-matrix composites, AIP Conf. Proc. 370 (1) (1996) 555–558.
[29] G.T. Gray III, R.S. Hixson, J.N. Johnson, Dynamic deformation and fracture response of a 6061-T6 Al–50 vol.% Al_2O3 continuous reinforced composite, AIP Conf. Proc. 370 (1) (1996) 547–550.
[30] V.V. Karakulov, I.Y. Smolin, Metal-ceramic materials. Study and prediction of effective mechanical properties, AIP Conf. Proc. 1760 (1) (2016), 020024.
[31] I.A. Zhukov, G.V. Garkushin, S.A. Vorozhtsov, A.P. Khrustalyov, S.V. Razorenov, A.V. Kvetinskaya, V.V. Promakhov, A.S. Zhukov, Special features of the mechanical characteristics of Al-Al_2O_3 composites produced by explosive compaction of powders under shock-wave deformation, Russ. Phys. J. 58 (9) (2016) 1358–1361.
[32] B.X. Bie, J.Y. Huang, D. Fan, T. Sun, K. Fezzaa, X.H. Xiao, M.L. Qi, S.N. Luo, Orientation-dependent tensile deformation and damage of a T700 carbon fiber/epoxy composite: a synchrotron-based study, Carbon 121 (2017) 127–133.
[33] H.W. Chai, H.Y. Li, X.H. Xiao, J.Y. Huang, S.N. Luo, Correlation between cell wall buckling and deformation banding in a closed-cell foam, Scripta Mater. 170 (2019) 177–182.
[34] H.Y. Li, H.W. Chai, X.H. Xiao, J.Y. Huang, S.N. Luo, Fractal breakage of porous carbonate sand particles: microstructures and mechanisms, Powder Technol. (2020) 112–121.
[35] H.W. Chai, Z.L. Xie, X.H. Xiao, H.L. Xie, J.Y. Huang, S.N. Luo, Microstructural characterization and constitutive modelling of deformation of closed-cell foams based on in situ x-ray tomography, Int. J. Plast. (2020) 102730.

[36] S.J. Ye, H.W. Chai, X.H. Xiao, Y. Cai, X.H. Yao, S.N. Luo, Spallation of polycarbonate under plate impact loading, J. Appl. Phys. 126 (8) (2019), 085105.
[37] J. Krautkrämer, H. Krautkrämer, Ultrasonic Testing of Materials, Springer Science, New York, 1990.
[38] L. Ma, J.Y. Liu, C. Li, Z.Y. Zhong, L. Lu, S.N. Luo, Effects of alloying element segregation bands on impact response of a 304 stainless steel, Mater. Char. 153 (2019) 294–303.
[39] M. Jafari, M.H. Enayati, M.H. Abbasi, F. Karimzadeh, Thermal stability and structural changes during heat treatment of nanostructured Al2024 alloy, J. Alloys Compd. 478 (1–2) (2009) 260–264.
[40] C.F. Deng, D.Z. Wang, X.X. Zhang, A.B. Li, Processing and properties of carbon nanotubes reinforced aluminum composites, Mater. Sci. Eng. A 444 (1–2) (2007) 138–145.
[41] Y. Sun, H. Cui, L. Gong, J. Chen, P.K. Shen, C.X. Wang, Field nanoemitter: one-dimension Al_4C_3 ceramics, Nanoscale 3 (7) (2011) 2978–2982.
[42] M.S. Dresselhaus, G. Dresselhaus, R. Saito, A. Jorio, Raman spectroscopy of carbon nanotubes, Phys. Rep. 409 (2) (2005) 47–99.
[43] G.M. Scamans, E.P. Butler, In situ observations of crystalline oxide formation during aluminum and aluminum alloy oxidation, Metall. Trans. A 6 (11) (1975) 2055–2063.
[44] Y. Ma, X. Zhou, G.E. Thompson, T. Hashimoto, P. Thomson, M. Fowles, Distribution of intermetallics in an AA 2099-T8 aluminium alloy extrusion, Mater. Chem. Phys. 126 (1–2) (2011) 46–53.
[45] A. Daoud, J.B. Vogt, E. Charkaluk, J. Bouquerel, L. Zhang, J.C. Biasci, Anisotropy effects on the tensile and fatigue behaviour of an oxide dispersion strengthened copper alloy, Mater. Sci. Eng. A 534 (2012) 640–648.
[46] J.W. Geng, G. Liu, F.F. Wang, T.R. Hong, C.J. Xia, M.L. Wang, D. Chen, N.H. Ma, H.W. Wang, Microstructural and mechanical anisotropy of extruded in-situ TiB_2/2024 composite plate, Mater. Sci. Eng. A 687 (2017) 131–140.
[47] R.C. Chen, D. Dreossi, L. Mancini, R. Menk, L. Rigon, T.Q. Xiao, R. Longo, PITRE: software for phase–sensitive X-ray image processing and tomography reconstruction, J. Synchrotron Radiat. 19 (5) (2012) 836–845.
[48] A.K. Zurek, W.R. Thissell, J.N. Johnson, D.L. Tonks, R. Hixson, Micromechanics of spall and damage in tantalum, J. Mater. Process. Technol. 60 (1) (1996) 261–267.
[49] J.C. Cheng, H.Y. Li, C. Li, X.H. Xiao, Z.Y. Zhong, L. Lu, S.N. Luo, Effects of second-phase boron particles on impact response of aluminum, Mater. Sci. Eng. A (2020) 139805.
[50] G.I. Kanel, Spall fracture: methodological aspects, mechanisms and governing factors, Int. J. Fract. 163 (1–2) (2010) 173–191.
[51] M.A. Meyers, Dynamic Behavior of Materials, John Wiley & Sons, New York, 1994.
[52] C. Li, B. Li, J.Y. Huang, H.H. Ma, M.H. Zhu, J. Zhu, S.N. Luo, Spall damage of a mild carbon steel: effects of peak stress, strain rate and pulse duration, Mater. Sci. Eng. A 660 (2016) 139–147.
[53] S.P. Marsh, LASL Shock Hugoniot Data, Univ. of California Press, Berkeley, 1980.
[54] S.N. Luo, Q. An, T.C. Germann, L.B. Han, Shock-induced spall in solid and liquid Cu at extreme strain rates, J. Appl. Phys. 106 (1) (2009), 013502.
[55] G.I. Kanel, A.V. Utkin, Estimation of the spall fracture kinetics from the free-surface velocity profiles, AIP Conf. Proc. 370 (1) (1996) 487–490.
[56] K.D. Joshi, A. Rav, A. Sur, T.C. Kaushik, S.C. Gupta, Spall fracture in aluminium alloy at high strain rates, AIP Conf. Proc. 1731 (1) (2016), 060013.
[57] J. Bontaz-Carion, Y.P. Pellegrini, X-ray microtomography analysis of dynamic damage in tantalum, Adv. Eng. Mater. 8 (6) (2006) 480–486.
[58] Y. Yao, H.W. Chai, C. Li, B.X. Bie, X.H. Xiao, J.Y. Huang, M.L. Qi, S.N. Luo, Deformation and damage of sintered low-porosity aluminum under planar impact: microstructures and mechanisms, J. Mater. Sci. 53 (6) (2018) 4582–4597.
[59] B.X. Bie, J.H. Han, L. Lu, X.M. Zhou, M.L. Qi, Z. Zhang, S.N. Luo, Dynamic fracture of carbon nanotube/epoxy composites under high strain-rate loading, Compos. Appl. Sci. Manuf. 68 (2015) 282–288.
[60] A.M.K. Esawi, K. Morsi, A. Sayed, A.A. Gawad, P. Borah, Fabrication and properties of dispersed carbon nanotube-aluminum composites, Mater. Sci. Eng. A 508 (1–2) (2009) 167–173.
[61] S.R. Bakshi, A. Agarwal, An analysis of the factors affecting strengthening in carbon nanotube reinforced aluminum composites, Carbon 49 (2) (2011) 533–544.
[62] A. Agarwal, S.R. Bakshi, D. Lahiri, Carbon Nanotubes: Reinforced Metal Matrix Composites, CRC Press, Boca Raton, 2010.
[63] J.P. Escobedo, D. Dennis-Koller, E.K. Cerreta, B.M. Patterson, C.A. Bronkhorst, B.L. Hansen, D. Tonks, R.A. Lebensohn, Effects of grain size and boundary structure on the dynamic tensile response of copper, J. Appl. Phys. 110 (3) (2011), 033513.